Discriminating healthy from tumor and necrosis tissue in rat brain tissue samples by Raman spectral imaging

Nadia Amharref [a], Abdelilah Beljebbar [a,*], Sylvain Dukic [a], Lydie Venteo [b], Laurence Schneider [b], Michel Pluot [b], Michel Manfait [a]

[a] Unité MéDIAN, CNRS-UMR 6142, UFR de Pharmacie, IFR 53, Université de Reims Champagne-Ardenne, 51 rue Cognacq-Jay, 51096 Reims Cedex, France
[b] Laboratoire Central d'Anatomie et de Cytologie Pathologiques, CHU Robert Debré, Avenue du Général Koenig, 51092 Reims Cedex, France

Abstract

The purpose of this study was to investigate molecular changes associated with glioma tissues by Raman microspectroscopy in order to develop its use in clinical practice. Spectroscopic markers obtained from C6 glioma tissues were compared to conventional histological and histochemical techniques. Cholesterol and phospholipid contents were highest in corpus callosum and decreased gradually towards the cortex surface as well as in the tumor. Two different necrotic areas have been identified: a fully necrotic zone characterized by the presence of plasma proteins and a peri-necrotic area with a high lipid content. This result was confirmed by Nile Red staining. Additionally, one structure was detected in the periphery of the tumor. Invisible with histopathological hematoxylin and eosin staining, it was revealed by immunohistochemical Ki-67 and MT1-MMP staining used to visualize the proliferative and invasive activities of glioma, respectively. Hierarchical cluster analysis on the only cluster averaged spectra showed a clear distinction between normal, tumoral, necrotic and edematous tissues. Raman microspectroscopy can discriminate between healthy and tumoral brain tissue and yield spectroscopic markers associated with the proliferative and invasive properties of glioblastoma. Development of in vivo Raman spectroscopy could thus accurately define tumor margins, identify tumor remnants, and help in the development of novel therapies for glioblastoma.

1. Introduction

In spite of clinical and technological advances in the understanding and treatment of glioma, the survival of patients has not notably improved. Indeed, malignant glioma produces profound and progressive disability leading to death in most cases. Moreover, these tumors remain mostly refractory to standard therapies (such as surgery, radiotherapy and conventional chemotherapy), and new therapeutic approaches are clearly needed [1].

Surgery remains the most commonly used therapeutic approach. However, complete resection of the tumor is only carried out in less than 20% of patients, highlighting the difficulty in clearly defining tumoral limits during surgery due to its invasive nature [2–5]. In order to improve drug treatments and to facilitate their clinical evaluation, it thus appears capital to find new markers defining tumoral margins through biology or medical imaging. As such, the development of a methodology enabling grading and prognosis of glioma would be of clinical benefit.

Raman spectroscopy is a vibrational spectroscopic technique with a high molecular specificity that can be used in medical diagnostics [6]. This technique has been successfully applied in the diagnosis of cancers such as those of the skin, breast, oesophagus, colorectum, and urogenital tract [7]. Raman spectra, resulting from inelastic scattering of light by the molecules present in a sample, provide information about the molecular composition, molecular structures, and molecular interactions in a tissue. They also reflect changes in the molecular composition and structures associated with disease. The success of Raman spectroscopy as a biomedical tool lies in its potential for in vivo applications and its ability to guide real-time therapeutic interventions.

---

* Corresponding author. Tel.: +33 3 2691 8376; fax: +33 3 2691 3550.
  E-mail address: abdelilah.beljebbar@univ-reims.fr (A. Beljebbar).

Mizuno et al. analyzed Raman spectra from different anatomical and functional structures of rat brain, and were the first to publish spectra of different brain tumors [8,9]. Recently, several Raman studies have been published that constitute a basis for subsequent studies to develop classification models for diagnosis of human brain tumor [10,11]. Moreover, Krafft et al. suggested the use Raman spectroscopy as a diagnostic tool to distinguish normal from tumoral tissue, and to determine the tumor type and grade [12]. Therefore, the purpose of our study was to use Raman spectroscopic imaging to discriminate between healthy and tumoral tissue and to identify spectroscopic markers associated with tumor progression and invasion, as well as tumor growth and necrosis. This study will help in the future development of in vivo Raman spectroscopy to accurately define tumor margins, to identify tumor remnants and to develop novel therapies for glioblastoma.

2. Materials and methods

2.1. Animal procedures

All animal procedures adhered to the "Principles of laboratory animal care" (NIH publication #85-23, revised 1985). Male Wistar rats weighing 409 ± 85 g (mean $\pm$ SD) were purchased from Harland (Paris, France). All animals were kept individually in standard animal facilities (20 ± 2 °C; $65 \pm 15\%$ relative humidity) and maintained under a 12:12 h light/dark cycle. They were given free access to food (Harlan Tecklad, France) and water throughout the study.

The C6 glioma tumor line used in this study and the cell inoculation procedure have been described elsewhere [13]. Briefly, rats were anesthetized with isoflurane and placed into a stereotactic head holder (Phymep, France). A small burr hole was drilled into the right side of the skull (anterior 1 mm; lateral 3 mm; lateral depth 4 mm, according to the bregma). Then, a tumor cell suspension (5.10^6 cells in 10 μl DMEM/NUT.MIX.F-12) was injected with a syringe over 2 min. After tumor cell implantation, the hole was closed with bone wax, and rats allowed to recover from anaesthesia.

2.2. Sample handling and preparation

Twenty days after tumor cell injection, control and tumor-bearing rats were sacrificed. After brain excision, tissue samples were snap-frozen by immersion in methyl-butane cooled down in liquid nitrogen and stored at −80 °C. For Raman spectroscopic studies, 15-μm-thick brain sections were made with a cryotome and placed onto calcium fluoride slides (CaF_2). After Raman measurements, all tissues were hematoxylin and eosin (H&E) stained to provide direct comparison of the Raman mapping results to histopathology.

2.3. Ki-67 immunostaining

Tissues were fixed in 10% buffered formalin, routinely processed, and embedded in paraffin. Immunohistochemical studies were performed on 3- to 6-μm-thick sections. Sections were deparaffinized and subjected to heat-induced epitope retrieval by steaming for 10 min. Slides were then incubated at 4°C overnight with an antibody recognizing the nuclear antigen Ki-67 (Rabbit Monoclonal, 1:200; Labvision Corporation, UK). Antibodies were detected using universal immuno-peroxidase polymer for rat tissue sections anti-mouse and anti-rabbit primary antibodies (N-Histofine Simple Stain Rat MAX PO, Nichirei Corporation, Japan). Amygdale tissue was used as a positive control. Healthy brain tissue served as the negative control. Sections were counterstained with hematoxylin.

2.4. MT1-MMP Immunostaining

Tumor sections (3–4 μm thick) were cut from formalin-fixed, paraffin embedded brain tissue. They were hydrated through graded alcohols and incubated in H_2O_2 (3% 10 min). They were then subjected to heat-induced epitope retrieval in citrate buffer (pH 6) by steaming for 10 min (Dako, Glostrup, Denmark). Sections were treated with the primary mouse anti-human-MT1-MMP monoclonal antibody, whose expression correlates with tumor invasion, (113-5B7, 1:100, Fuji Chemical Industries, Japan) for 24 h in the cold. They were then treated for 30 min at room temperature with universal immuno-peroxidase polymer for rat tissue sections anti-mouse and anti-rabbit primary antibodies (N-Histofine Simple Stain Rat MAX PO, Nichirei Corporation, Japan). Healthy brain tissue served as the negative control. Sections were counterstained with hematoxylin.

2.5. Nile red staining

Stock solutions of Nile red (500 μg/ml) were prepared by dissolving Nile blue A chloride (Cl 51180; Sigma-Aldrich, Saint Quentin Fallavier, France) in acetone and stored chilled and protected from light. Fresh solutions of Nile red were made by adding 2–10 μl of the stock solution to 1 ml of 75% glycerol followed by brisk vortexing. The glycerol-dye solution was then briefly degassed by vacuum.

To stain frozen sections (6–10 μm thick), a drop of the glycerol staining solution was added to each section and the preparation covered with a glass coverslip. After 1 h, sections were examined by fluorescence microscopy at two spectral settings: yellow-gold fluorescence and red fluorescence. As such, neutral lipids were seen as yellow-gold fluorescent structures; whereas the red fluorescent structures, which are yellow-gold fluorescence negative, were mainly composed of phospholipids, other amphipathic lipids, and strongly hydrophobic proteins of cell membranes.

2.6. Reference Raman spectra

Raman reference spectra were obtained from specific lipids dissolved in chloroform and placed onto a CaF_2 slide. The following chemicals were purchased from Sigma-Aldrich (Saint Quentin Fallavier, France) and used without further purification: Cholesterol (99%), phosphatidylcholine (1,2-diacyl-sn-glycero-3-phosphocholine, 99%, from egg yolk), phosphatidylethanolamine (1,2-dihexadecanoyl-sn-glycero-3phosphoethanolamine, 99%), sphingomyelin (N-acyl-D-sphingosine-1-phosphocholine, 99%, from bovine brain), galactocerebroside (ceramide β-D-galactoside, 99%, from bovine brain).

2.7. Raman spectroscopy

Raman spectra of tissue sections were recorded with a near infrared confocal Raman microspectrometer (Labram, Horiba Jobin Yvon S.A.S., France). The setup consisted of a microscope (Olympus, HB40, France) coupled to the Labram spectrometer. The microscope was equipped with a xy-motorized (Marzhauser, Germany), computer-controlled sample stage, which enabled automatic scanning of the sample with a resolution of 1 μm. The excitation source (785 nm) was provided by a titanium-sapphire laser (Model 3900S, Spectra-Physics, France) pumped with an Argon ion laser. The laser power on the sample was around 160 mW. This laser light was focused on the sample with a 100× optimized objective (Olympus, France). This objective collected light that was scattered by the sample, which was then analyzed by the spectrometer equipped with a Pelletier-cooled charge-coupled device detector. The Raman signal was collected using 5 s of signal collection time per Raman pixel in the 600- to 1800-cm^{-1} spectral region with a spectral resolution of 4 cm^{-1}. For our measurements, the objective was set on autofocus. This system allowed focusing the laser light on each point of the tissue section. Unstained cryosections were placed on the microscope. A screen image recorder camera attached to the microscope enabled the acquisition of the white light multi-image of the area under investigation. Raman maps were recorded by defining a scanning xy-step size of 50 μm as controlled by the LabSpec software (Horiba Jobin Yvon S.A.S. France). The 100× objective collected light on a 3- to 4-μm spot. The xy-step size was chosen based on previous studies (unpublished results) that showed that higher resolution Raman maps with a 15-μm xy-step size did not bring any additional information than those measured with a 50-μm step size.

2.8. Spectroscopic data analysis

Raman data were analyzed with custom software developed in MatLab (MathWorks, Inc., Matick, USA). After acquisition, spectra were first calibrated using Raman calibration standards [14]. The spectrum of the halogen lamp was

used to correct for the wavelength-dependent signal detection efficiency of the Raman setup. Spectral pre-treatment also involved subtraction of the interfering background Raman signal originating from the optical elements in the laser light delivery pathway, the CaF_2 slide, and the interfering glue biopolymer used during freezing.

Raman maps were constructed from the spectral data using multivariate statistical techniques. Data were first scaled using a Standard Normal Variate (SNV) transformation [15]. As such, every spectrum was mean centered (so that the average of the spectral intensities in all wavenumber channels was set to zero) and scaled to have a standard deviation of one. Principal component analysis (PCA) was used to identify the independent sources of variation in all spectra and to reduce the number of variables describing the data set. An unsupervised classification method (k-means cluster analysis) was then used to find groups of spectra that shared similar spectral characteristics. Thirty PCA scores, accounting for 99.9% of the captured variance, served as input for the unsupervised classification methods. The cluster-membership information was then plotted as a pseudo-color map by assigning a color to each different cluster. Pseudo-color Raman maps were then compared with histopathology results using HE-stained tissue sections. Positive difference spectra between clusters describing normal and tumor tissue structures were computed to determine the inter-cluster variance. These cluster average spectra were then used as input for hierarchical cluster analysis using Ward's clustering algorithm and the square Euclidian distance measure. This method was used to identify the discriminant characteristics between normal and tumor brain tissues.

3. Results

Raman Maps were obtained from unstained frozen sections of normal and glioma tumor tissues. Pseudo-color maps were constructed after multivariate statistical analysis (PCA, clustering analysis) and compared to histopathology results in order to correlate each pseudo-color with its anatomical counterpart. The aim of this method was to identify common and specific structures in normal and tumor brain tissues, and to spatially visualize these structures in the pseudo-color maps. Twelve clusters describing both healthy and cancer features were extracted, and pseudo Raman maps were constructed with the same color scale (white color representing areas where no tissue was present). In some samples, Raman maps and microscopic images of the H&E stained section were found to correlate well. In other samples, information complimentary to histopathology was obtained from cluster analysis leading to a better identification of the molecular changes associated with brain tissue alteration.

3.1. Healthy brain tissue

An example of the results of a Raman mapping experiment on normal brain tissue is shown in Fig. 1E. In this pseudo-color map, seven or twelve clusters were sufficient to describe all brain features. Comparison of this pseudo-color map with the microscopic image of the stained tissue section (Fig. 1A) enabled identification of the anatomical structures of the rat brain. As such, the area associated to the spatial distribution of cluster 9 correlates with white matter tissue from the corpus callosum (CC). Tissue surrounding CC was encoded by cluster 12. Other clusters (1, 3, 8, and 10) described the cortex (Gray matter). Clusters 2 and 7 described blood and could be associated to the vascularisation. Cluster averaged Raman spectra are shown in the same figure (Fig. 1). All extracted models exhibited bands of proteins and lipids as the main constituents of brain tissue. The band at 718 cm^{-1} can be assigned to phospholipids such as phosphati-

dylethanolamine (Fig. 2f) and/or phosphatidylcholine (Fig. 2h). The band at 1002 cm^{-1} was assigned to the aromatic amino-acid phenylalanine. Bands at 1062, 1128, and 1296 cm^{-1} correspond to aliphatic side chains, the band near 926 cm^{-1} to the C−C bond of the peptidic backbone, and bands at 1266 and 1658 cm^{-1} to the amide III and amide I vibrations of the peptidic backbone, respectively. All major protein bands at 1266, 1296, 1436 and 1658 cm^{-1} strongly overlap with lipid bands. All spectra corresponding to normal brain structures were characterized by a specific variability in those peak positions and intensities.

Positive difference spectra between clusters describing normal structures were computed to determine the changes between clusters averaged spectra (Fig. 2). These spectra give a good estimation of molecular species present in a relatively high amount in one spectrum as compared to the other. The difference spectrum between cluster 9 associated to CC and cluster 12 corresponding to adjacent tissue is presented in Fig. 2a. This spectrum shows bands at 700 cm^{-1}, 1062 cm^{-1} (C−O stretching and C−O−C symmetric stretching), 1128 cm^{-1} (C−C stretching), 1266 cm^{-1} (in plane CH_2 deformation), 1296 cm^{-1} (CH_2 and wagging), 1436 cm^{-1} (CH_2 bending), and 1670 cm^{-1} (C=C stretching). This difference spectrum contains a combination of bands that are characteristic of cholesterol (Fig. 2e) and phospholipids, especially phosphatidylethanolamine and galactocerebroside (Fig. 2f and g, respectively).

Comparison between pseudo-color map and the histopathology image (Fig. 1E and A) shows that the Raman image provides more information than standard histopathology staining in the cortex. As such, four layers were identified from the cortex, whereas H&E staining did not allow to discriminate these layers. Difference spectra between these cortex layers (Fig. 2b, c, and d) obtained by subtracting models spectra of successive layers (clusters 12-10, 10-1, and 1-3 respectively) were calculated. Comparison of these difference spectra showed that the band located at 700 cm^{-1}, characteristic of cholesterol, decreased from spectrum b to spectrum d (Fig. 2) suggesting that cholesterol content decreased gradually from CC to cortex, and even disappeared in the upper cortex layers. On the other hand, phospholipids bands, more pronounced in trace b, tended to decrease in traces c and d.

3.2. Brain tumor tissue

Molecular changes associated with malignant rat brain tumor were investigated. Fig. 1F to H show Raman maps of glioma brain tissues. These pseudo-color maps share some common structures with normal tissue such as CC (cluster 9), and cortex (clusters 1, 3, 10, and 12). Since the molecular composition of tissue is altered by tumor invasion, other clusters were assigned to tumor tissue (clusters 4, 5, 6, 8, and 11). All clusters associated with tumor (see Fig. 1) showed a decrease in the intensity of the lipids bands at 700, 1062, 1128, and 1296 cm^{-1} corresponding to cholesterol and phospholipids. In contrast, other bands were more pronounced in the tumor model such as bands at 782 and 826 cm^{-1} attributed to DNA and/or RNA. As shown in Fig. 1, comparison of pseudo-color maps (F, G, and H) with their respective histopathological images (B, C, and D) revealed that clusters 5 and 6 (blue and red
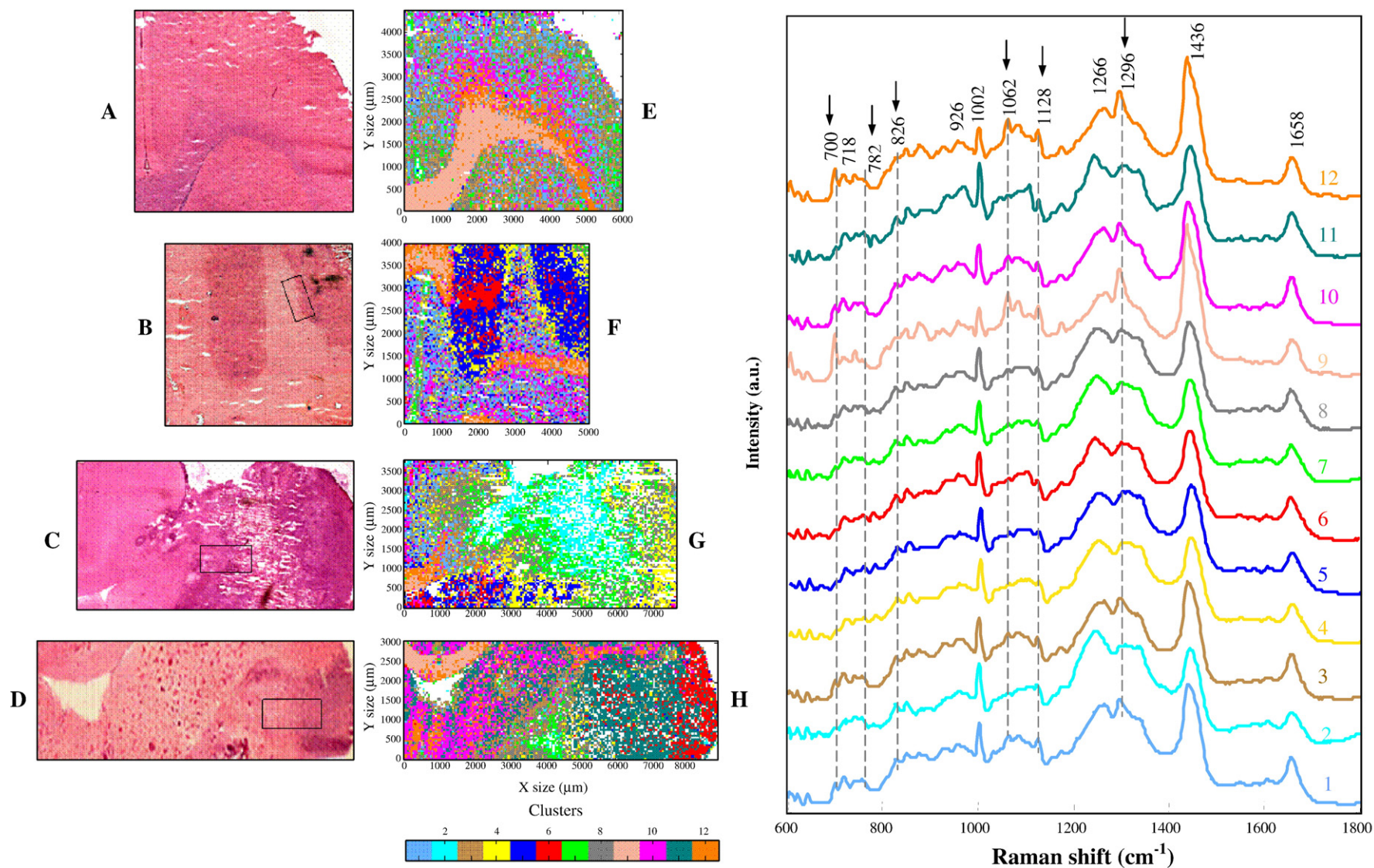
Fig. 1. Photomicrographs (H&E staining) of healthy (A) and glioma (B–D) brain tissue sections. Pseudocolor Raman maps E–H are based on 12-means cluster analysis on sections A–D, respectively. As per contra, representative cluster-averaged Raman spectra collected from healthy and glioma brain tissue sections. Spectra are shown with the same color than in the pseudocolor maps E–H.
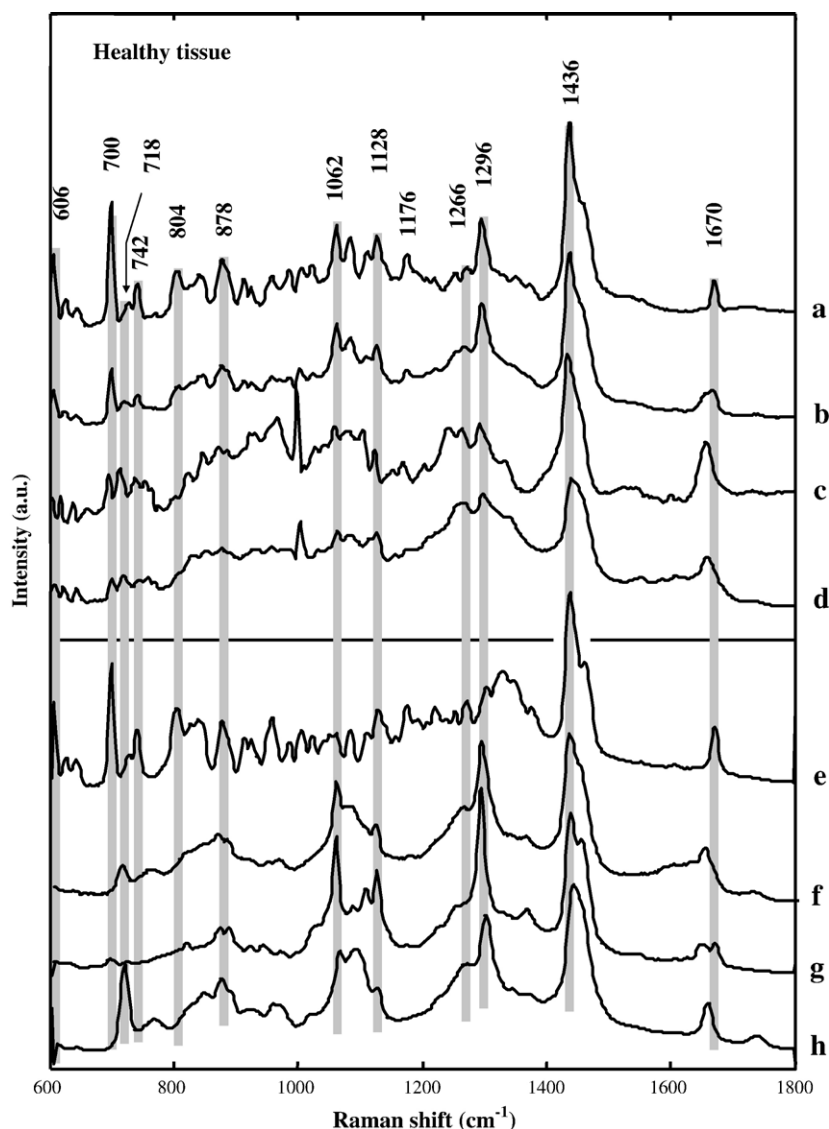
Fig. 2. Positive difference between cluster averaged spectra associated to healthy tissue. (a) Cluster 9 minus cluster 12; (b) Cluster 12 minus cluster 10; (c) Cluster 10 minus cluster 1; (d) Cluster 1 minus cluster 3. Raman spectra of pure compounds. (e) Cholesterol; (f) Phosphatidylethanolamine ; (g) Galactocerebroside; (h) Phosphatidylcholine.

color, respectively) correspond to the tumor area, whereas cluster 4 (yellow color) encodes the surrounding tumor. Moreover, a particular region described by cluster 11 (Fig. 1H) was identified.

To find molecular species that are only present in normal but not in tumor tissue and vice versa, two positive difference spectra between normal and tumor models were calculated. Fig. 3a displays the difference spectrum between cluster 1 (describing a cortex layer) and cluster 5 (associated to tumor). This spectrum showed a high lipid content, in particular cholesterol (band at $700 \ cm^{-1}$) and phosphatidylcholine and/or phosphatidylethanol-amine (bands at 718, 1128, 1296, and $1734 \ cm^{-1}$). Other changes involve the presence of bands at 782, 826, and $1104 \ cm^{-1}$ attributed to DNA conformation. On the other hand, analysis of the difference spectrum between cluster 5 and cluster 1 (Fig. 3b), similar to that of blood (Fig. 3f), showed a major protein content. To identify the molecular changes between tumor (cluster 5) and its surrounding area, a difference spectrum (cluster 4 minus cluster 5)

was calculated. The resulting spectrum (Fig. 3c) was comparable to that of blood (Fig. 3f). To determine the particular structure described by cluster 11, a difference spectrum between cluster 11 and tumor (cluster 5) was calculated (see Fig. 3d). This difference spectrum, as it possesses bands similar to those of plasma (Fig. 3e), shows that cluster 11 could be assigned to edema, a result in agreement with the anatomopathologist's opinion. Incidentally, the H&E examination of the section showed interstitial spaces characteristic of extracellular fluid volume enlargement (Fig. 4D).

To better understand the specific spectral changes associated with healthy and diseased states of tissue, comparisons between pseudo-color Raman maps and immunostaining were performed. Immunohistochemistry pointed out that the proliferation activity of tumors can be assessed by means of Ki-67 staining, a technique commonly used in clinical pathology and neuropathology diagnostics. Fig. 4A shows Ki-67 staining of the area defined by a black frame in Fig. 1B. It reveals an important nuclear
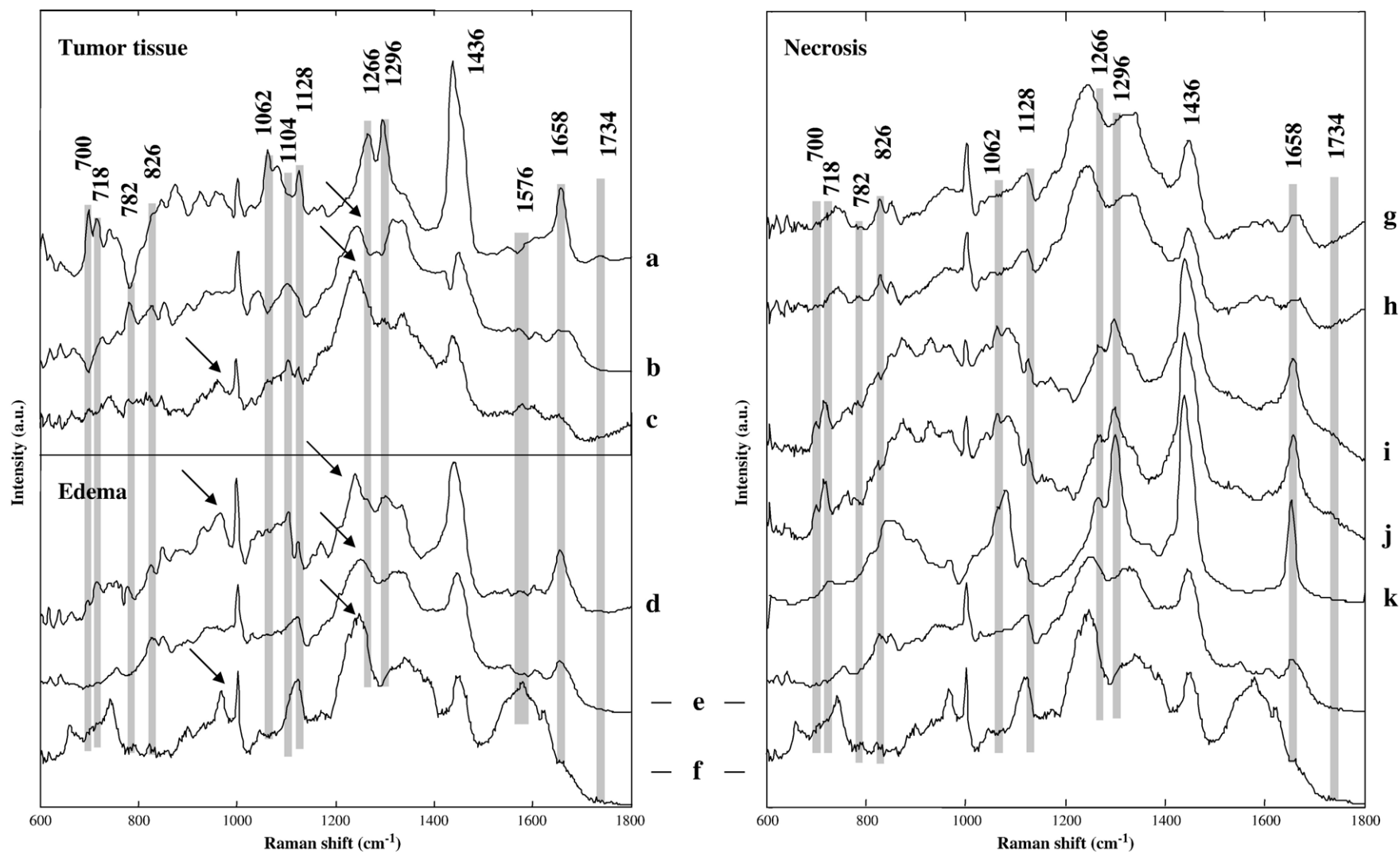
Fig. 3. Positive difference between cluster averaged spectra associated to tumor tissue. (a) Cluster 1 minus cluster 5; (b) cluster 5 minus cluster 1; (c) cluster 4 minus cluster 5; (d) cluster 11 minus cluster 5; Raman spectra of (e) plasma and (f) blood. (g) Cluster 2 minus cluster 7; (h) cluster 7 minus cluster 8; (i) cluster 8 minus cluster 2; (j) cluster 8 minus cluster 7. (k) Raman spectrum of Oleic acid.
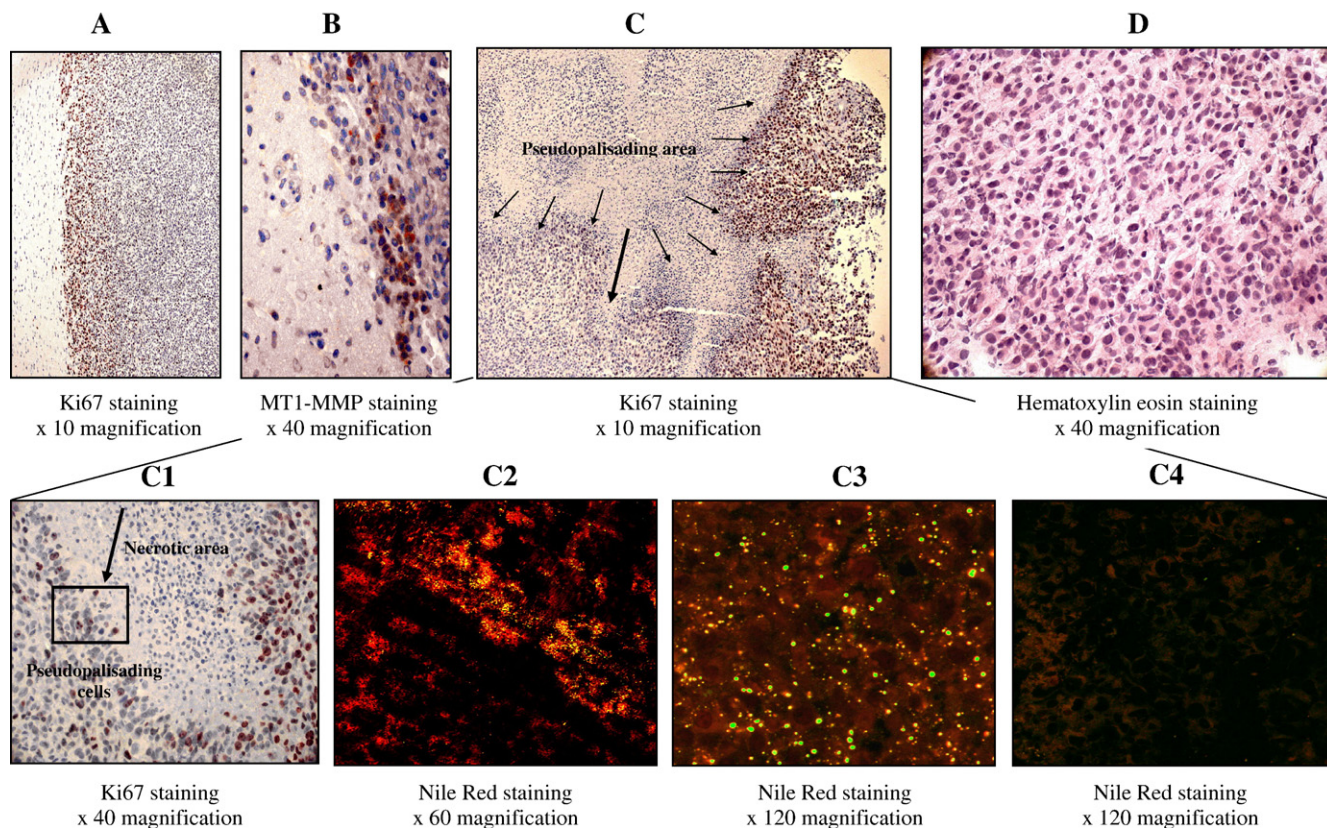
Fig. 4. Immunohistochemical staining (A) and (B) obtained on area marked with a black frame in Fig. 1B. (A) is a Ki-67 immunostaining demonstrating an increased staining in the area surrounding the tumor, (B) is a MT1-MMP immunostaining showing an increased expression of this metalloproteinase in tumor borders. Immunohistochemical staining (C) and (D) obtained on area marked with a black frame in Fig. 1C and D, respectively. (C) and (C1) are Ki67 immunostaining pointing out the pseudopalisading area. Fluorescence confocal microscopic images (C2), (C3) of the perinecrotic zone, and (C4) of the central necrotic zone, after Nile red staining. (D) H&E staining of edema zone.

labeling in the tumor border, suggesting a high proliferation activity of the cells from the area surrounding the tumor associated to cluster 4. To correlate this proliferative activity with the tumor invasion, MT1-MMP immunostaining was performed. Fig. 4B shows MT1-MMP staining on the same area, pointing out an over-expression of MT1-MMP by the peripheral tumor cells associated to the aggressive invasiveness of these tumor cells. The correlation between immunohistochemistry staining results and spectroscopic data shows the potential of Raman spectroscopy to identify spectroscopic markers associated with proliferative and invasive properties of glioblastoma. Ki-67 immunostaining of the tumor section (corresponding to the area marked by the black frame in Fig. 1C), as displayed in Fig. 4C, revealed two important areas: (i) a central necrotic area with a total absence of proliferation associated with pycnotic cells, blood components and cellular debris and, (ii) pseudopalisading cells with lower Ki-67 proliferation indices associated with the perinecrotic area (Fig. 4C1). Necrotic area and perinecrotic zones were associated to clusters 2, 7, and 8 (see Fig. 1G).

Difference spectra between cluster 2 and cluster 7 (Fig. 3g) as well as between cluster 7 and cluster 8 (Fig. 3h) were similar to that of plasma (Fig. 3e), suggesting the presence of blood in the center of the necrotic area and in the region associated with proliferative activity. On the other hand, difference spectra between cluster 8 and cluster 2 (Fig. 3i) and between cluster

8 and cluster 7 (Fig. 3j) were similar to that of oleic acid (Fig. 3k) with an additional band at 700 cm^{-1} associated with cholesterol. To identify the nature and the distribution of these lipids in tissue, Nile red staining was used. This technique revealed in the perinecrotic area the presence of phospholipids and neutral lipids (red fluorescence structures and yellow-gold labelling respectively; Fig. 4C2) associated with the presence of lipid droplets with a diameter of about 0.5 to 1 µm (visible in Fig. 4C3 with high magnification). Fig. 4C4, however, illustrates an absence of neutral lipids in the fully necrotic zone and the poor staining of the necrotic and pycnotic cells characterized by an altered cytoplasm and condensed nuclear. Nile red staining results were in agreement with those obtained by Raman spectroscopy showing a more important lipid distribution for cluster 8 than for clusters 2 and 7. In fact, the center of the necrosis (full necrosis) seems to correspond to cluster 2, whereas the peri-necrotic and necrotic zones (pseudopalisading and pycnotic cells, respectively) seem to be encoded by cluster 7 and 8.

To distinguish between normal, tumor, and necrotic brain structures, cluster averaged spectra obtained from pseudo-color maps were input in the hierarchical cluster analysis. The result, as shown on the dendrogram in Fig. 5, showed a clear distinction between all normal and tumor brain structures. Indeed, in the cluster-averaged spectra of normal brain structures, two sub-clusters associated with white matter (clusters 9 and 12
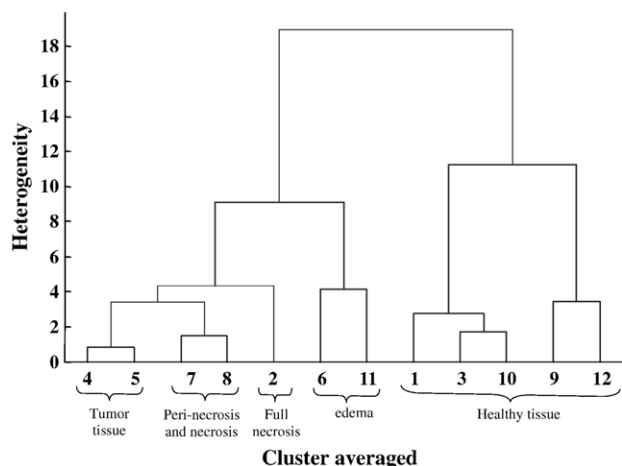
Fig. 5. Dendrogram obtained from hierarchical cluster analysis on spectral cluster averages associated to different tissue types. Heterogeneity represents the discriminating distance given by arbitrary units (au).

corresponding to higher cholesterol content) and grey matter (clusters 1, 3, and 10 with a lower cholesterol content) were discriminated. We were also able to discriminate between glioma (clusters 4, 5), peri-necrosis and necrosis (clusters 7 and 8), full necrosis (cluster 2), and edema (clusters 11 and 6) in the second groups.

4. Discussion

Our results demonstrate the potential of Raman microspectroscopic imaging to successfully discriminate between healthy and tumor tissue, and to characterize the invasive, necrotic, and edematous regions. The C6 rat glioma model was chosen because of its similar morphology to glioblastoma multiform, its rapid proliferative rate, and its reproducibility, criteria often desired for an in vivo experimental brain tumor [16–18]. Raman maps allowed clear identification of the anatomical structures of the healthy rat brain (CC and cortex), and visualization of the changes associated with tumor and necrosis. Healthy cerebral parenchyma was characterized by an important lipid content, whereas tumor tissue was characterized by an important protein content. Pseudo-color maps allowed a clear modeling of all cerebral structures such as CC and cortex. The difference spectrum between CC and adjacent tissue contained a combination of bands characteristic of cholesterol, phosphatidylethanolamine and/or phosphatidylcholine and galactocerebroside, in agreement with the data of Krafft et al. [12]. These lipids are essential components of myelin which contains high molar percentages of cerebroside, cerebroside sulphate, and cholesterol [19–21]. The proportions of cholesterol and galactocerebroside decreased gradually from CC towards the surface of the cortex. This gradient is related to myelin content as found in various cortical layers [22] in a previous study using luxol fast blue staining to visualize myelin distribution in brain tissue and to map particular cortex sections [13].

Tumor development was characterized by a reduction in total lipid content, including cholesterol. This result, in agreement with those obtained in brain diseases [23], is correlated with demy-

elination. This lowering in lipid content in malignant tissues might be related to the fast growth of tumor cells which need more energy [24]. Indeed, it is known that in developing brain tumors, structural and functional cell changes take place in which lipids play a crucial role. Yet, qualitative and quantitative aspects of lipid changes in brain tumors of different degrees of malignancy are still the subject of numerous studies [25]. Using Infrared microspectroscopy, Krafft et al. have evaluated the usefulness of the lipid-to-protein ratio (2850/1655 cm^{-1}) as a spectroscopic marker to discriminate between normal and tumor tissue, as well as between low- and high-grade glioma tissues. They demonstrated that this ratio is maximal for normal brain tissue and decreases with the progression of the disease [25]. In general, an increase in malignancy is accompanied by a reduction in total lipids that involves all main classes of lipids found in plasma membranes [26]. Changes in lipid and in phospholipids content, as seen in glioblastoma as compared with adjacent tissue, could indicate an evolution in the undergoing pathological process. Increased levels of cholesterol esters (cholesterol oleate and linoleate) have also been reported in glioma tissue [10]. Koljenoviv et al. demonstrated that the difference between meningioma and dura is mainly related to lipids, cholesterol linoleate and linoleic acid levels. Steiner et al. studied the discriminating constituents between normal and tumoral tissues (astrocytoma and glioblastoma) by infrared spectroscopy. They demonstrated that changes mainly arise from differences in lipid constituents. The potential use of lipid measurements for judging the stage, and hence the prognosis, of low-grade tumors is suggested by the apparent gradual increase in lipid content over time. This increase, believed to be associated with necrosis, could thus be used in low-grade tumors as an early marker of disease prior to the patient becoming symptomatic [27–29].

Glioblastoma is the most malignant brain tumor as it aggressively proliferates and invades surrounding normal brain tissues. Ki-67 and MT1-MMP staining associated with the proliferative and invasive activities of glioblastoma, respectively, were clearly correlated with cluster 4 that encoded the surrounding area. In fact, previous work showed that MT1-MMP is expressed on the surface of rat C6 glioblastoma cells as its metalloproteolytic activity is required to overcome myelin's inhibitory effect on cell migration [30]. The lack of MT1-MMP expression in normal brain (data not shown) indicates that MT1-MMP expression is abnormally activated in neoplastic glial cells, and thus suggests that overexpression of MT1-MMP might facilitate tumor invasiveness through the activation of MMP-2 [31]. The correlation between immunohistochemistry staining results and spectroscopic data shows the potential of Raman spectroscopy to provide spectroscopic markers associated with the proliferative and invasive properties of glioblastoma. This finding is very important for future developments of in vivo Raman spectroscopy to accurately define tumor margins, to identify tumor remnants in glioma, and to help in the development of novel therapies for glioblastoma [32].

A particular cluster (cluster 11) needs to be highlighted. This cluster, which is located in tumor and in tissue adjacent to the tumor (i.e. Caudate Putamen), displays characteristics of blood spectra, and particularly of plasma. It is now well known that brain tumors alter the permeability of the blood–brain barrier,

which leads to extravasation of a protein-rich plasma filtrate into the interstitial space with subsequent accumulation of vascular fluid [33]. Vasogenic edema, the most common type of edema associated with brain tumors, is found in both grey and white matter, and is located in extracellular spaces. Histological study of H&E stained sections revealed an enlargement of the extracellular fluid volume which provides an evidence of brain edema [34]. The latter is one of the most important factors leading to morbidity and mortality associated with brain tumors. By definition, brain edema is characterized by an increase in brain volume resulting from increased water, sodium and serum protein content. In the difference spectrum between edema (cluster 11) and tumor (cluster 5), several bands were associated to plasma proteins and could thus be used as spectroscopic markers to identify the edema. Hydrostatic and osmotic forces encourage the movement of fluid out of the vascular compartment into the parenchyma resulting in a mass effect. Brain compression leads to abnormal diffusion of nutrients which results in acidosis, hypoxia, and inflammatory changes. The edema fluid contains serum proteins and various bioactive substances released by the tumor [35] which can damage the tissue [36]. To our knowledge, this is the first time that an identification of the tumoral and associated tumoral edema was carried out by Raman microspectroscopy. In a preceeding article [13], we described a particular structure located around the tumor that was associated with peritumoral edema. Raman imaging thus confirmed these results previously obtained by infrared spectroscopy.

The presence of necrosis is important for grading tumors, and is often linked to a poorer clinical prognosis [37,38]. Therefore, we attempted to identify the necrotic part of the glioma. In this glioblastoma model, two different regions were identified: the center of the necrotic zone and a peri-necrotic and necrotic zone. Raman spectra revealed the presence of blood in the center of necrotic zones and a high lipid content in the peri-necrotic zones. As such, necrosis, induced by different stimuli including hypoxia, is accompanied by ion and water efflux and dispersal of organelles, coming from membrane cell rupture [39], and the necrotic core is a result of hypoxia [40]. The most necrotic part of the tumor was characterized by the presence of plasma proteins (due to edema) and of proteins from the cytoplasm of necrotic cells. One pathological feature that distinguishes glioblastoma from lower grade astrocytomas and which can explain the abrupt change in biological behaviour is the presence of pseudopalisading necrosis, a dense collection of neoplastic cells surrounding a central necrotic focus. In fact, the presence of pseudopalisading necrosis and the increased levels of angiogenesis, markers of glioblastoma, are pathophysiologically linked and mechanistically instrumental to disease progression [41–43]. Nile red staining was used to identify the nature and the distribution of lipids in these tissues. Our results demonstrate that cells surrounding necrosis contain lipid droplets (neutral lipids). Non-lipid droplets were also found in the central part of necrosis that could be related to the extent of the necrotic zone. Previous studies using magnetic resonance spectroscopy have reported the presence of lipid droplets in C6 glioma and in human brain tumors [44–47], and their presence has been attributed to the rapid tumoral growth [48]. The central part of necrosis was mainly composed of

proteins, and Raman spectra reflected the presence of plasmatic compounds. This result is in agreement with the extravasation of plasma proteins as found in glioma [35].

There are only a few studies using vibrational spectroscopy for the characterization of necrosis [49,28]. Koljenvic et al. have discriminated vital from necrotic glioblastoma tissues by Raman microspectroscopy. They demonstrated that necrotic tissue contains higher levels of cholesterol than vital tumor tissue. Yamada et al. came to the same conclusions by comparing necrotic and vital carcinoma tissues [49]. Our tumor models were characterized by a large necrotic area with complete necrosis in the center. The necrotic zones were very heterogeneous and could be graded as either complete or partial. Neutral lipids were absent from the completely necrotic region (as confirmed by Nile red staining) whereas they were more commonly found in the peri-necrotic zone.

Our study shows the ability of Raman spectroscopy to accurately diagnose normal, tumoral, and necrotic tissue *ex-vivo*. For *ex-vivo* measurements, Raman microspectroscopy, in which high NA microscopic lenses are employed, allows measurements with a high spatial resolution and good signal collection efficiency. Recent developments in optic fiber probes now enable signal collection times of about 1 s, a time short enough for medical applications [50,51]. A recent study has demonstrated the potential of Raman spectroscopy for real-time margin assessment during partial mastectomy surgery by providing detailed quantitative chemical information of tissue margins [51]. This modelling approach is based on the assumptions that the Raman spectrum measured on breast tissue is a linear combination of the spectra of its individual tissue components. The comparison between tissue composition extracted from normal and tumor through modelling (the fit coefficient) was used to diagnose morphological and structural changes associated with disease.

5. Conclusion

The combination of Raman microspectroscopy with multivariate analysis has a clear potential in providing an objective diagnostic complimentary to that obtained by histopathology, and can lead to a better understanding of the molecular changes associated with tumor. In this study, we successfully discriminated between normal structures, tumoral, peri-tumoral, necrotic, and edematous zones in brain tissue. Structural changes were mainly related to qualitative and quantitative changes in lipid content that can be used as spectroscopic markers for this pathology. Additionally, a particular cluster was found and attributed to edema in agreement with the histopathologist's opinion. By combining spectral results with Ki-67 and MT1-MMP immunohistochemical staining, the proliferative and invasive activities of glioblastoma can be detected in the periphery of the tumor tissue. Two different regions were identified in the necrotic part of the glioma: a center mainly associated to plasma proteins, and a peri-necrotic zone containing a high proportion of lipid droplets.

References

[1] L.M. DeAngelis, Brain tumors, N. Engl. J. Med. 344 (2001) 1114–1123.

[2] B.K. Rasheed, R.N. Wiltshire, S.H. Bigner, Molecular pathogenesis of malignant gliomas, Curr. Opin. Oncol. 11 (1999) 162–167.

[3] A. Giese, R. Bjerkvig, M.E. Berens, M.J. Westphal, Cost of migration: invasion of malignant gliomas and implications for treatment, Clin. Oncol. 21 (2003) 1624–1636.

[4] F.K. Albert, M. Forsting, K. Sartor, H.P. Adams, S. Kunze, Early postoperative magnetic resonance imaging after resection of malignant glioma: objective evaluation of residual tumor and its influence on regrowth and prognosis, Neurosurgery 34 (1994) 45–61.

[5] A. Kowalczuk, R.L. Macdonald, C. Amidei, G. Dohrmann, R.K. Erickson, J. Hekmatpanah, S. Krauss, S. Krishnasamy, G. Masters, S.F. Mullan, A.J. Mundt, P. Sweeney, E.E. Vokes, B.K.A. Weir, R.L. Wollman, L.D. Lunsford, D.G.T. Thomas, K. Takakura, P.H. Gutin, P.M. Black, M.L.J. Apuzzo, Quantitative imaging study of extent of surgical resection and prognosis of malignant astrocytomas, Neurosurgery 41 (1997) 1028–1038.

[6] L.P. Choo-Smith, H.G. Edwards, H.P. Endtz, J.M. Kros, F. Heule, H. Barr, J.S. Robinson, H.A. Bruining, G.J. Puppels, Medical applications of Raman spectroscopy: from proof of principle to clinical implementation, Biopolymers 67 (2002) 1–9.

[7] R. Jyothi Lakshmi, V.B Kartha, C.R. Murali Krishna, J.G. Solomon, G. Ullas, P. Uma Devi, Tissue Raman spectroscopy for the study of radiation damage: brain irradiation of mice, P. Radiat. Res. 157 (2002) 175–182.

[8] A. Mizuno, T. Hayashi, K. Tashibu, S. Maraishi, K. Kawauchi, Y. Ozaki, Near-infrared FT-Raman spectra of the rat brain tissues, Neurosci. Lett. 141 (1992) 47–52.

[9] A. Mizuno, H. Kitajima, K. Kawauchi, S. Muraishi, Y.J. Ozaki, Near infrared Fourier transform Raman spectroscopic study of human brain tissues and tumours, Raman Spectrosc. 25 (1994) 25–29.

[10] S. Koljenovic, L.P. Choo-Smith, T.C. Bakker Schut, J.M. Kros, H.J. van den Berge, G. Puppels, Discriminating vital tumor from necrotic tissue in human glioblastoma tissue samples by Raman spectroscopy, Lab. Invest. 82 (2002) 1265–1277.

[11] C. Krafft, S.B. Sobottka, G. Schackert, R. Salzer, Near infrared Raman spectroscopic mapping of native brain tissue and intracranial tumors, Analyst 130 (2005) 1070–1077.

[12] C. Krafft, L. Neudert, T. Simat, R. Salzer, Near infrared Raman spectra of human brain lipids, Spectrochim. Acta 61 (2005) 1529–1535 (Part A).

[13] N. Amharref, A. Beljebbar, S. Dukic, L. Venteo, L. Schneider, M. Pluot, R. Vistelle, M. Manfait, Brain tissue characterisation by infrared imaging in a rat glioma model, Biochim. Biophys. Acta 1758 (2006) 892–899.

[14] R. Wolthuis, R. Schut, T.C. Bakker, P.J. Caspers, H.P.J. Buschman, T.J. Romer, H.A. Bruining, G.J. Puppels, Raman spectroscopic methods for in vitro and in vivo tissue characterization, in: W.T. Mason (Ed.), Fluorescent and Luminescent Probes, 2nd ed., Academic Press, London, 1999, pp. 433–455.

[15] R.J. Barnes, M.S. Dhanoa, S.J. Lister, Standard normal variate transformation and detrending of near-infrared diffuse reflectance spectra, Appl. Spectrosc. 43 (1989) 772–777.

[16] J.J. Bernstein, W.J. Goldberg, E.R. Laws, D. Conger, V. Morreale, L.R. Wood, C6 glioma cell invasion and migration of rat brain after neural homografting: ultrastructure, Neurosurgery 26 (1990) 622–628.

[17] P. Menei, M. Boisdron-Celle, A. Croue, G. Guy, J.P. Benoit, Effect of stereotactic implantation of biodegradable 5-fluorouracil-loaded microspheres in healthy and C6 glioma-bearing rats, Neurosurgery 39 (1996) 117–124.

[18] S.F. Dukic, M.L. Kaltenbach, T. Heurtaux, G. Hoizey, A. Lallemand, R. Vistelle, Influence of C6 and CNS1 brain tumors on methotrexate pharmacokinetics in plasma and brain tissue, J. Neurooncol. 67 (2004) 131–138.

[19] J.S. O'Brien, E.L. Sampson, Lipid composition of the normal human brain: gray matter, white matter, and myelin, J. Lipid Res. 6 (1965) 537–544.

[20] G. Saher, B. Brugger, C. Lappe-Siefke, W. Mobius, R. Tozawa, M.C. Wehr, F. Wieland, S. Ishibashi, K.A. Nave, High cholesterol level is essential for myelin membrane growth, Nat. Neurosci. 8 (2005) 468–475.

[21] A.G. Tzakos, A. Troganis, V. Theodorou, T. Tselios, C. Svamas, J. Matsoukas, V. Apostolopoulos, I.P. Gerothanassis, Structure and function of the myelin proteins: current status and perspectives in relation to multiple sclerosis, Curr. Med. Chem. 12 (2005) 1569–1587.

[22] R.D. Burwell, Borders and cytoarchitecture of the perirhinal and postrhinal cortices in the rat, J. Comp. Neurol. 437 (2001) 17–41.

[23] J. Kneipp, P. Lasch, E. Baldauf, M. Beekes, D. Naumann, Detection of pathological molecular alterations in scrapie-infected hamster brain by Fourier transform infrared spectroscopy, Biochim. Biophys. Acta 1501 (2000) 189–199.

[24] J.S. Wang, J.S. Shi, Y.Z. Xu, X.Y. Duan, L. Zhang, S.F. Weng, J.G. Wu, FT-IR spectroscopic analysis of normal and cancerous tissues of esophagus, World J. Gastroenterol. 9 (2003) 1897–1899.

[25] C. Krafft, K. Thummler, S.B. Sobottka, G. Schackert, R. Salzer, Classification of malignant gliomas by infrared spectroscopy and linear discriminant analysis, Biopolymers 82 (2006) 301–305.

[26] R. Campanella, Membrane lipids modifications in human gliomas of different degree of malignancy, J. Neurosurg. Sci. 36 (1992) 11–25.

[27] C. Krafft, S.B. Sobottka, G. Schackert, R. Salzer, Analysis of human brain tissue, brain tumors and tumor cells by infrared spectroscopic mapping, J. Raman Spectrosc. 37 (2006) 367–375.

[28] S. Koljenovic, T.B. Schut, A. Vincent, J.M. Kros, G.J. Puppels, Discriminating vital tumor from necrotic tissue in human glioblastoma tissue samples by Raman spectroscopy, Anal. Chem. 77 (2005) 7958–7965.

[29] G. Steiner, A. Shaw, L.P. Choo-Smith, G. Schackert, W. Steller, H.M. Abuid, R. Salzer, Distinguishing and grading human gliomas by infrared spectroscopy, Biopolymers 72 (2003) 464–471.

[30] A.T. Belien, P.A. Paganetti, M.E. Schwab, Membrane-type 1 matrix metalloprotease (MT1-MMP) enables invasive migration of glioma cells in central nervous system white matter, J. Cell Biol. 144 (1999) 373–384.

[31] M. Yamamoto, S. Mohanam, R. Sawaya, G.N. Fuller, M. Seiki, H. Sato, Z.L. Gokaslan, L.A. Liotta, G.L. Nicolson, J.S. Rao, Differential expression of membrane-type matrix metalloproteinase and its correlation with gelatinase A activation in human malignant brain tumors in vivo and in vitro, Cancer Res. 56 (1996) 384–392.

[32] M. Yamamoto, Y. Ueno, S. Hayashi, T. Fukushima, The role of proteolysis in tumor invasiveness in glioblastoma and metastatic brain tumors, Anticancer Res. 22 (2002) 4265–4268.

[33] T. Hurter, Experimental brain tumors and edema in rats. II. Tumor edema, Exp. Pathol. 26 (1984) 41–48.

[34] J. Meixensberger, M. Bendszus, K. Licht, L. Solymosi, K. Roosen, Peritumoural brain oedema: diagnosis and treatment approaches, CNS Drugs 13 (2000) 233–251.

[35] T. Ohnishi, P.B. Sher, J.B. Posner, W.R. Shapiro, Increased capillary permeability in rat brain induced by factors secreted by cultured C6 glioma cells: role in peritumoral brain edema, J. Neurooncol. 10 (1991) 13–25.

[36] Y. Ikeda, D.M. Long, Oxygen free radicals in the genesis of peritumoural brain oedema in experimental malignant brain tumours, Acta Neurochir. Suppl. 51 (1990) 142–144.

[37] E.C. Alvord, Is necrosis helpful in the grading of gliomas? Editorial opinion, J. Neuropathol. Exp. Neurol. 5 (1992) 127–132.

[38] F.G. Barker, R.L. Davis, S.M. Chang, M.D. Prados, Necrosis as a prognostic factor in glioblastoma multiforme, Cancer 77 (1996) 1161–1166.

[39] A.H. Wyllie, E. Duvall, in: J.O. McGee, P.G. Isaacson, N.A. Wright (Eds.), Textbook of Pathology, Oxford University Press, Oxford, 1992, pp. 141–157.

[40] D.J. Brat, E.G. Van Meir, Vaso-occlusive and prothrombotic mechanisms associated with tumor hypoxia, necrosis, and accelerated growth in glioblastoma, Lab. Invest. 84 (2004) 397–405.

[41] D.J. Brat, A.A. Castellano-Sanchez, S.B. Hunter, M. Pecot, C. Cohen, E.H. Hammond, S.N. Devi, B. Kaur, E.G. Van Mier, Pseudopalisades in glioblastoma are hypoxic, express extracellular matrix proteases, and are formed by an actively migrating cell population, Cancer Res. 64 (2004) 920–927.

[42] Y. Sonoda, T. Ozawa, Y. Hirose, K.D. Aldape, M. McMahon, M.S. Berger, R.O. Pieper, Formation of intracranial tumors by genetically modified human astrocytes defines four pathways critical in the development of human anaplastic astrocytoma, Cancer Res. 61 (2001) 4956–4960.

[43] Y. Rong, D.E. Post, R.O. Pieper, D.L. Durden, E.G. Van Meir, D.J. Brat, PTEN and hypoxia regulate tissue factor expression and plasma coagulation by glioblastoma, Cancer Res. 65 (2005) 1406–1413.

[44] H. Lahrech, S. Zoula, R. Farion, C. Remy, M. Decorps, In vivo measurement of the size of lipid droplets in an intracerebral glioma in the rat, Magn. Reson. Med. 45 (2001) 409–414.

[45] S. Zoula, G. Herigault, A. Ziegler, R. Farion, M. Decorps, C. Remy, Correlation between the occurrence of 1H-MRS lipid signal, necrosis and lipid droplets during C6 rat glioma development, NMR Biomed. 16 (2003) 199–212.

[46] W.G. Negendank, R. Sauter, T.R. Brown, J.L. Evelhoch, A. Falini, E.D. Gotsis, A. Heerschap, K. Kamada, B.C. Lee, M.M. Mengeot, E. Moser, K.A. Padavic-Shaller, J.A. Sanders, T.A. Spraggins, A.E. Stillman, B. Terwey, T.J. Vogl, K. Wicklow, R.A. Zimmerman, Proton magnetic resonance spectroscopy in patients with glial tumors: a multicenter study, J. Neurosurg. 84 (1996) 449–458.

[47] P.E. Sijens, M. Oudkerk, P. van Dijk, P.C. Levendag, C.J. Vecht, 1H MR spectroscopy monitoring of changes in choline peak area and line shape

after Gd-contrast administration, Magn. Reson. Imaging 16 (1998) 1273–1280.

[48] M.E. Meyerand, J.M. Pipas, A. Mamourian, Classification of biopsy-confirmed brain tumors using single-voxel MR spectroscopy, AJNR Am. J. Neuroradiol. 20 (1999) 117–123.

[49] T. Yamada, N. Miyoshi, T. Ogawa, K. Akao, M. Fukuda, T. Ogasawara, Y. Kitagawa, K. Sano, Observation of molecular changes of a necrotic tissue from a murine carcinoma by Fourier-transform infrared microspectroscopy, Clin. Cancer Res. 8 (2002) 2010–2014.

[50] T.C. Bakker Schut, M.J. Witjes, H.J. Sterenborg, O.C. Speelman, J.L. Roodenburg, E.T. Marple, H.A. Bruining, G.J. Puppels, In vivo detection of dysplastic tissue by Raman spectroscopy, Anal. Chem. 15 (2000) 6010–6018.

[51] A.S. Haka, Z. Volynskaya, J.A. Gardecki, J. Nazemi, J. Lyons, D. Hicks, M. Fitzmaurice, R.R. Dasari, J.P. Crowe, M.S. Feld, In vivo margin assessment during partial mastectomy breast surgery using Raman spectroscopy, Cancer Res. 15 (66) (2006) 3317–3322.